Original Article

Trans-polyacetylene based organic spin valve for a multifunctional spin-based device: A first principle analysis

Kumar Gaurav [a], Boddepalli SanthiBhushan [b], Gonzalo Gutierrez [c], Rajeev Ahuja [d, e], Anurag Srivastava [a, *]

[a] Advanced Materials Research Group, CNT Laboratory, ABV - Indian Institute of Information Technology and Management, Gwalior, M.P., India
[b] Department of Electronics and Communication Engineering, Indian Institute of Information Technology, Allahabad, U.P., India
[c] Group of Nano Materials, Department of Physics, University of Chile, Santiago, Chile
[d] Condensed Matter Theory Group, Department of Physics and Astronomy, Uppsala University, Uppsala, Sweden
[e] Department of Physics, Indian Institute of Technology, Ropar, Punjab, India

ARTICLE INFO

ABSTRACT

Carbon-based materials are the promising candidates for the design of multifunctional spintronic devices, owing to their fascinating inherent attributes such as the ballistic transport nature, long spin coherence time, etc. Here, we report the spin-dependent electron transport properties of a trans-polyacetylene channel sandwiched between two semi-infinite hydrogen-passivated zigzag graphene nanoribbon (ZGNR) electrodes within the framework of spin-polarized density functional theory (DFT) and non-equilibrium Green's function (NEGF) formalisms. The proposed device exhibits an excellent spin-dependent transport behavior within the bias window of [-0.5 V, 0.5 V]. In parallel configuration (PC), the device offers an ideal spin filtration efficiency of almost 100% within the bias range of [-0.4 V, 0.4 V], and in antiparallel configuration (APC), it exhibits negative differential resistance (NDR), dual-spin rectification, and dual-spin filtration effects. Also, a high tunnel magnetoresistance (TMR) of 1.2×10^5% is achieved. To validate the aforementioned effects, the transmission spectra along with the area enclosed by the curve, eigenvalues, eigenstates, and quantum conductance have also been analyzed. In addition, the impact of hybridization and torsion defects on the spin-dependent transport phenomenon through trans-polyacetylene has been investigated. Furthermore, the modelled device is observed to exhibit the spin Seebeck effect in PC under the influence of temperature gradient. The proposed device may stand as a good contender for various spintronic and spin caloritronic applications.

© 2022 Vietnam National University, Hanoi. Published by Elsevier B.V. This is an open access article under the CC BY-NC-ND license (http://creativecommons.org/licenses/by-nc-nd/4.0/).

1. Introduction

Spintronics is an emerging multidisciplinary domain in nano-technology that deals with an electron's spin-dependent properties besides its charge-dependent properties [1–3]. An addition of spin as a degree of freedom offers new capabilities, effects, and functionalities to the device. Spintronics came to light by the advent of giant magnetoresistance (GMR) in 1988 while studying a Fe/Cr/Fe multilayer system [4]. Over the past few decades, spin-based devices such as spin valves [5–7] and spin field effect transistors [8,9]

have gained enormous attention from the research community in both theoretical and experimental domains. In particular, the spin valve research is at the forefront, owing to its vast applications in the field of magnetic sensors and information storage.

Spin valve has been the immediate outcome of GMR discovery. A metallic spin valve [5] was first realized at IBM research division lab in 1991 using non-magnetic metal (Cu, Ag, and Au) layer as spacer material. Here, they observed an in-plane magnetoresistance, and a relative change in resistance (ΔR) of 5% in 10 Oe at room temperature. However, it has certain limitations, such as insignal amplification and incompatibility with existing semiconductor technology. Later in 2002, Dediu et al. [10] reported the first experimental evidence of the direct spin polarized transport through an organic semiconductor, with a GMR of 30% and spin diffusion length of approximately 200 nm in Sexithienyl (T_6) organic molecule at room temperature. Soon after this discovery,

Xiong et al. [6] reported the first organic spin valve effect with a small π-conjugated molecule 8-hydroxy-quinoline aluminium (Alq$_3$) as spacer material. In this device, a GMR of 40% was obtained at 11 K that reaches zero as the temperature increases beyond 200 K, with an estimated spin diffusion length of 45 nm at 11 K. It has been discussed elsewhere that, the π-conjugated organic semiconductors made up of elements with lower atomic number can have remarkably weak spin−orbit interaction (SOI), and weak hyperfine interaction resulting in a very long spin relaxation time (spin diffusion length) [11−13]. Moreover, they may offer additional advantages over their counterparts, such as self-assembly process, tunable electronic structures, large spin coherence, and chemical flexibility. These findings suggest that the usage of organic molecules may not be limited to organic spin valves [7,14,15], but also for spin photoresponse devices [16] and spin-OLEDs [17].

Over the years, researchers have paid special attention to the carbon-based spintronics, owing to their fascinating transport and spin attributes. Rocha et al. [14] modeled an organic spin valve by using octane and tricene in tunnelling and metallic regimes, respectively, and also demonstrated the molecule selection via. end-group engineering. Hill et al. [18] also reported similar spin valve effect in planar graphene, that shows a 10% change in resistance as the spin orientation of electrodes changes from PC to APC at 300 K and the applied field is swept between +450 G and −450 G. So far, various 1-D namomaterials and organic molecules have been explored, both experimentally and computationally to study its morphological impact on the spin valve effects. Zeng et al. [19] investigated the carbon atomic chain embedded between graphene nanoribbons for spintronic applications such as spin filter and spin valve. Sharko et al. [20] fabricated a multilayer spin valve using CoFeP/Cu-Magnetic nanowires, that offer a maximum GMR up to ~9%. The authors claimed the structure to be a promising candidate for the magnetic field sensor. Bordoloi et al. [21] developed a double quantum dot-spin valve (DQD-SV) using InAs nanowire with ferromagnetic split gates that results in a tunnel magnetoresistance (TMR), electrically tunable in a range of +80% and −90%. Recently, Zhou et al. [22] achieved a spin injection efficiency of 100% and a large TMR in graphene nanoribbons under transverse electric field.

Earlier, Gaurav et al. investigated [23] the influence of hybridization as well as torsion defects on the electron charge transport through trans-polyacetylene with homogeneous electrodes for both relaxed and external maximum tensile stress conditions. The present article explores the trans-polyacetylene based organic spin valve as a multifunctional device, particularly as a spin filter, spin diode, and spin-based oscillator. Trans-polyacetylene is basically a conducting polymer having n repetitive units of (-C=C-)$_n$, indicating inherent conjugation. It is an isomer of polyacetylene - a one-dimensional conjugated organic polymer. Polyacetylene is the simplest possible organic polymer having sp^2 hybridized carbon atoms, first reported in 1929 by Champetier from the polymerization of acetylene [24]. Trans-polyacetylene has been chosen for the present study as this possesses all the properties required for a spacer material of organic spin valves, owing to the π-conjugation and lower atomic number of constituent elements [6]. Earlier, trans-polyacetylene was also successfully utilized in various other applications such as solar cells [25] and mechanochemistry [26]. The present work further investigates the influence of different tunnel barrier lengths, hybridization defects (introduction of sp^3 hybridized carbon atom), and torsion defects on the spin-dependent transport phenomena of our device. Additionally,

spin-dependent transport under the influence of temperature gradient has also been studied for its possible application in the field of spin caloritronics [27,28].

This article is organized as follows. The next section elaborates the theoretical approach and computational details adopted for this work. Subsequently, the results and discussion section elaborates on the structural as well as electronic properties and spin-dependent transport under the influence of applied bias and temperature gradient.

2. Computational methods

The computation has been carried out using the spin-polarized density functional theory (DFT) [29] and non-equilibrium Green's function (NEGF) [30] formalism based ab-initio code, Synopsys-Quantum ATK [31]. The spin-dependent generalized gradient approximation [32] functional with Perdew−Burke−Ernzerhof parameterization has been employed to describe the exchange−correlation interaction energies of electrons, as it considers both the electron density and its gradient. The double-ζ-polarized basis sets have been chosen to expand the wave functions and to provide an accurate description of π conjugated bonds, with a sufficient grid mesh cutoff of 160 Ry. Before proceeding to the transport calculations, the device structure has been relaxed via. Limited-memory-Broyden-Fletcher-Goldfarb-Shanno (LBFGS) optimization process, such that the maximum residual force on each atom converges to below 0.05 eV Å^{-1}. Furthermore, a sufficient vacuum region was considered in the non-transport directions (i.e. along x and y-axis) to reduce the spurious interactions among neighboring supercells introduced by the periodic boundary conditions. The Monkhorst−Pack k-point sampling has been set to be $1 \times 1 \times 100$ for transport calculations. Here, two sets of device configurations have been considered, based on the initial magnetizations of left (source) and right (drain) electrodes. In parallel configuration (PC), both the electrodes have same alignment (or orientation) of spin. Whereas, in antiparallel configuration (APC), both the electrodes have opposite alignment of spin i.e. having a phase difference of $180°$.

The spin-polarized transmission coefficient ($T^{\uparrow(\downarrow)}(E, V)$) of the system at a particular bias voltage (V) is given by,

$$T^{\uparrow(\downarrow)}(E, V) = T_r[\Gamma_L(E, V)G^R(E, V)\Gamma_R(E, V)G^A(E, V)]^{\uparrow(\downarrow)} \tag{1}$$

Here, G^A and G^R indicate the advanced and retarded Green's functions, respectively. Γ_R and Γ_L are the coupling functions referring to the imaginary part of right and left electrode self-energies, respectively.

The above mentioned equation (1) is incorporated into the Landauer-Buttiker formula [33], to determine the spin-dependent current−voltage (I−V) characteristics of the device,

$$I^{\uparrow(\downarrow)} = \frac{2e}{h} \int_{\mu_R}^{\mu_L} T^{\uparrow(\downarrow)}(E, V)[f(E - \mu_L) - f(E - \mu_R)]dE \tag{2}$$

Here, h, e, and f(E) are the Planck's constant, elementary charge, and Fermi-Dirac distribution function, respectively. μ_R and μ_L are the chemical potentials of right and left electrodes, respectively. Additionally, the spin-dependent current under the influence of temperature gradient (ΔT) has been calculated in the PC configuration using $\Delta T = T_R - T_L$. Here, T_R and T_L correspond to the temperature of the right and left electrodes, respectively.

3. Results and discussion

3.1. Spin-dependent transport phenomena

For the detailed spin-dependent transport analysis, the structural and electronic properties of the device have been studied. The device schematic of trans-polyacetylene sandwiched between the two semi-infinite H-passivated ZGNR electrodes is shown in Fig. 1, where the measured lattice constant, C–C and C–H bond lengths, and width of the optimized ZGNR are in accordance with the literature [34,35]. The spin dependent band structure and DOS profiles of ZGNR electrodes reveal their magnetic metallic behavior [36] (See Fig. S1 and analysis provided in the supplementary information).

Moreover, the spin-dependent transmission spectrum for both the PC and APC at zero bias, is depicted in Fig. 2. From Fig. 2a, it can be seen that the equilibrium between two spin states got disturbed in the vicinity of Fermi level (E_F). The spin up and spin down states are available at different energy regions, thus resulting in a non-zero spin polarized current. Table 1 lists the maximum transmission coefficients at the E_F for PC and APC. In PC, the up spin states attain the maximum value and offer a large spin splitting energy, a crucial parameter for spin filtering phenomena.

Further, the spin-dependent transport properties of the modeled device in PC and APC configurations have been examined. The current–voltage (I–V) characteristics are computed for a bias range of −0.5 V–0.5 V and are plotted in Fig. 3. In PC configuration, the current through the device is highly spin-polarized (see Fig. 3a). The up spin current shows a symmetric behavior w.r.t origin, and increases linearly till ±0.3 V, thereafter decreases slowly with the applied bias voltage. In contrast, the spin down current is completely suppressed in both negative and positive sides of the bias window. It indicates that the modeled device allows the up spin electrons to propagate freely from the left electrode to the right electrode, prohibiting the down spin electron movement, thereby resulting in a perfect spin filtering behavior.

To further understand this behavior, the spin filtration efficiency (η) has been calculated in the PC, using the following equation (3):

$$\eta = \frac{I_\alpha - I_\beta}{I_\alpha + I_\beta} \times 100\% \tag{3}$$

Here, I_α and I_β correspond to the current due to majority and minority spins, respectively. In the present work, the majority and minority spins refer to the electrons' up and down spin components, respectively. At zero bias, as the current due to both the spin components is zero, hence the efficiency has been computed in terms of transmission coefficients, as shown in the equation (4):

$$\eta = \frac{T_\alpha(E_F) - T_\beta(E_F)}{T_\alpha(E_F) + T_\beta(E_F)} \times 100\% \tag{4}$$

Here, $T_\alpha(E_F)$ and $T_\beta(E_F)$ represent the majority and minority spin transmission coefficients at the Fermi level, respectively. Fig. 4a illustrates the spin filtration efficiency (η) as a function of bias potential in the PC, which shows an efficiency of almost 100% within the voltage range of [−0.4 V, 0.4 V]. This can also be attributed to the large spin-splitting energy near the Fermi level, as highlighted via. green arrows in Fig. 2a to indicate the energy range. To further justify the aforementioned effect and I−V characteristics in the PC, the area enclosed by the transmission coefficient (T(E)) curve at a particular bias voltage has also been extracted (See Fig. 4b). Here, the area enclosed by the up spin component is significantly higher than the down spin component and is symmetric w.r.t 0 V. Hence, the up spin current increases almost linearly and symmetrically, while the down spin current is mostly suppressed within the bias window. However, as the bias voltage increases from 0.4 V to 0.5 V, the area enclosed by up (down) spin component decreases (increases), resulting in a minor reduction of η value at 0.5 V as shown in Fig. 4a.

In APC configuration (see Fig. 3b), the up spin current is completely suppressed, whereas the down spin current raises from zero for the positive bias voltages above 0.2 V. This indicates the semiconducting behavior of the device in APC with a threshold voltage of 0.2 V, owing to the low transmission coefficients below the threshold voltage as depicted in Fig. 2b. On the negative side of the bias window, a completely opposite pattern is witnessed. Thus, both the up and down spin currents offer the rectification behavior in APC. In order to quantify the rectification effect, the rectification ratio has been calculated in the APC, by using the following equation (5):

$$RR = \frac{|I(\pm V)|}{|I(\mp V)|} \tag{5}$$

Here, I (+V) and I (-V) correspond to the current in positive and negative bias voltages, respectively. As shown in Fig. 5a, the rectification ratio increases with the bias voltage and reaches a
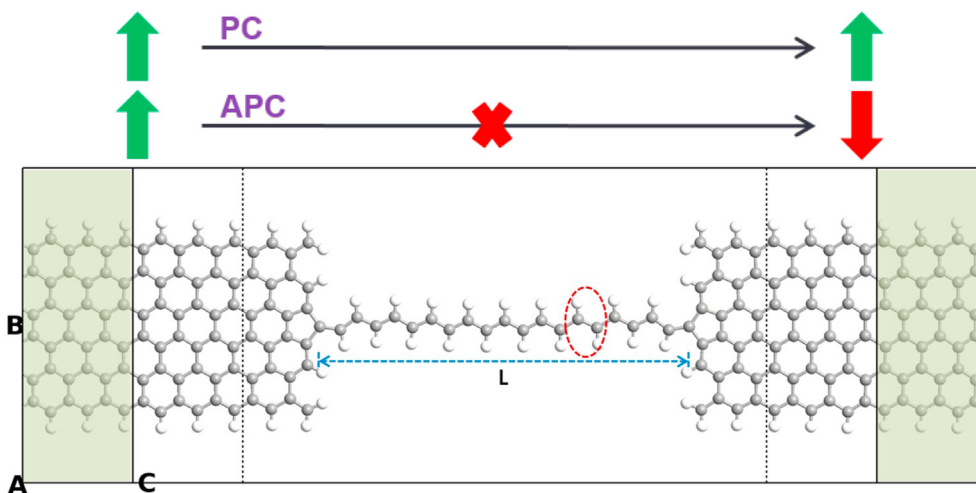

Fig. 1. A schematic device model of trans-polyacetylene sandwiched between two H-passivated ZGNR electrodes. (Here, the encircled section corresponds to the site for hybridization defect (Model IIA), and hybridization as well as torsion defects (Model IIB).).
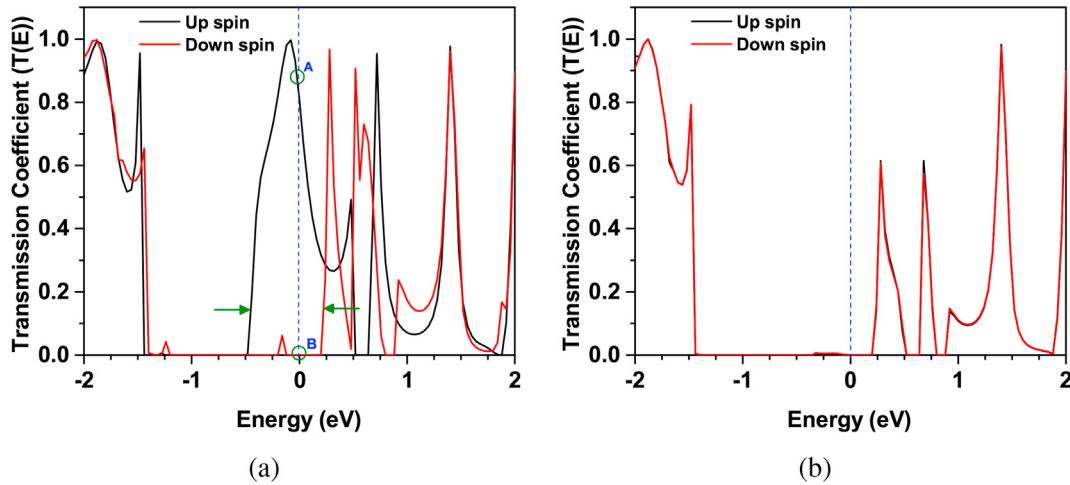
Fig. 2. Transmission Spectrum (at zero bias) in the (a) PC and (b) APC of the modeled device.

Table 1
Spin-transport properties in terms of T(E$_F$)$_{Max}$, quantum conductance (G), and transmission eigenvalues for both up and down spin channels in the PC and APC.

Configuration	T (E$_F$)$_{Max}$	G (μS)	Eigenvalues
PC-Up spin	8.78×10^{-1}	6.80×10^{1}	8.78×10^{-1}
PC-Down spin	8.28×10^{-8}	6.42×10^{-6}	8.28×10^{-8}
APC-Up spin	3.74×10^{-4}	2.90×10^{-2}	3.74×10^{-4}
APC-Down spin	3.70×10^{-4}	2.87×10^{-2}	3.70×10^{-4}

maximum of 416 and 436 for up and down spins, respectively, in the APC at 0.5 V. Moreover, the voltage-dependent η of APC oscillates between -17.45%, 23.63% for bias range -0.2 V-0.2 V (See supplementary information, Fig. S2). However, beyond ±0.2 V, the η increases gradually and achieves a maximum of almost $\pm100\%$ at ±0.5 V. It is worth mentioning that the down spin current is more dominant than the up spin current in the positive bias side, hence the η is negative; whereas the converse is true for the negative bias side. Both the rectification and filtering behavior in APC can be analyzed by carefully inspecting the plot depicting the area enclosed by the transmission coefficient (T(E)) curve for various bias voltages. From Fig. 4c, the area enclosed by both the spin components, is almost zero till ±0.2 V, then a spontaneous increase

in the area enclosed can be seen from ±0.3 V. In the positive bias side, the area enclosed by down spin component is significantly higher than the up spin component, whereas the converse is true in the negative bias side. Furthermore, NDR behavior is observed on the positive bias side (see Fig. 3b) for the down spin current, in the range of [0.4 V, 0.45 V] with a peak to valley ratio of 1.157. Here, the peak current (I$_P$) is 1.954 μA at 0.40 V and valley current (I$_V$) is 1.688 μA at 0.45 V. Similar NDR behavior can be seen for the up spin current on the negative bias side. These bias dependent NDR behaviors for up and down spin components suggest their possible application in the field of spin-based oscillators [37].

The above discussions reveal that the device displays distinct spin-dependent I−V characteristics in PC and APC. Therefore, the tunnel magnetoresistance (TMR) has been computed by using the 'optimistic approach' [38], as shown in equation (6):

$$TMR = \frac{I_{PC} - I_{APC}}{I_{APC}} \times 100\% \qquad (6)$$

Here, I$_{PC}$ and I$_{APC}$ indicate the total current (summation of up and down spin components) in PC and APC, respectively. However, the transmission coefficients have been considered for zero-bias TMR calculation, using the following equation (7):
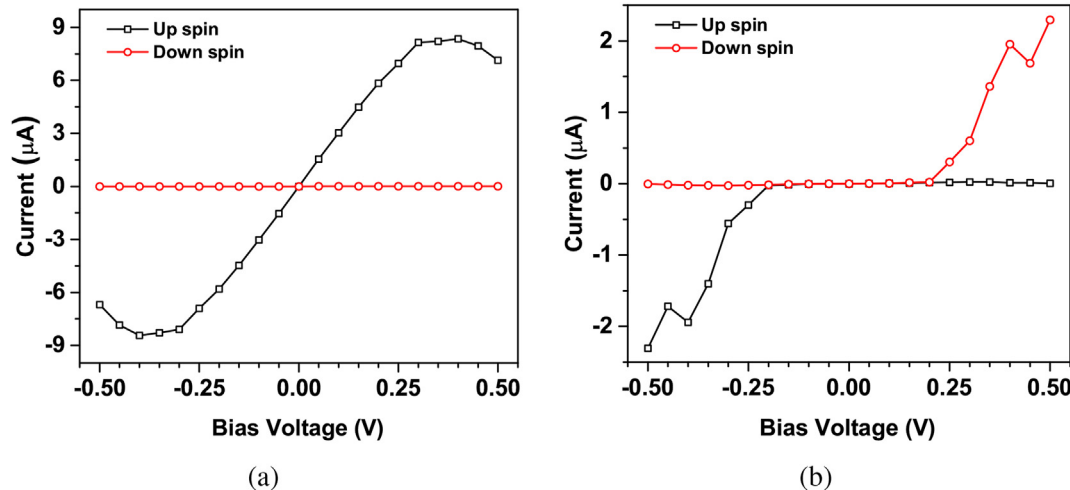

Fig. 3. Spin-dependent current as a function of bias potential for the modeled device (L = 24.91 Å) within the bias window of [-0.5 V, 0.5 V] in (a) PC and (b) APC.
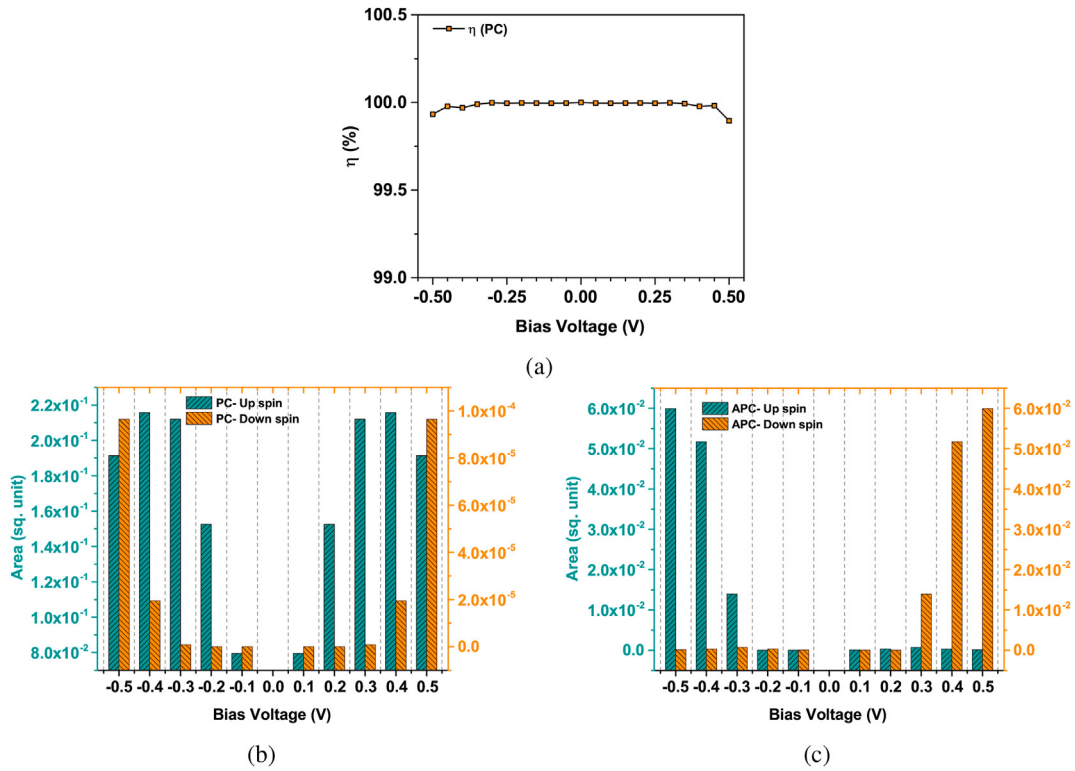
(a)

(b)　　　　　　　　　　　　　　　　　　　　　　　　　(c)

Fig. 4. (a) Spin filtration efficiency (η) in PC, and area enclosed by transmission spectrum T(E) for different bias voltages in (b) PC and (c) APC.

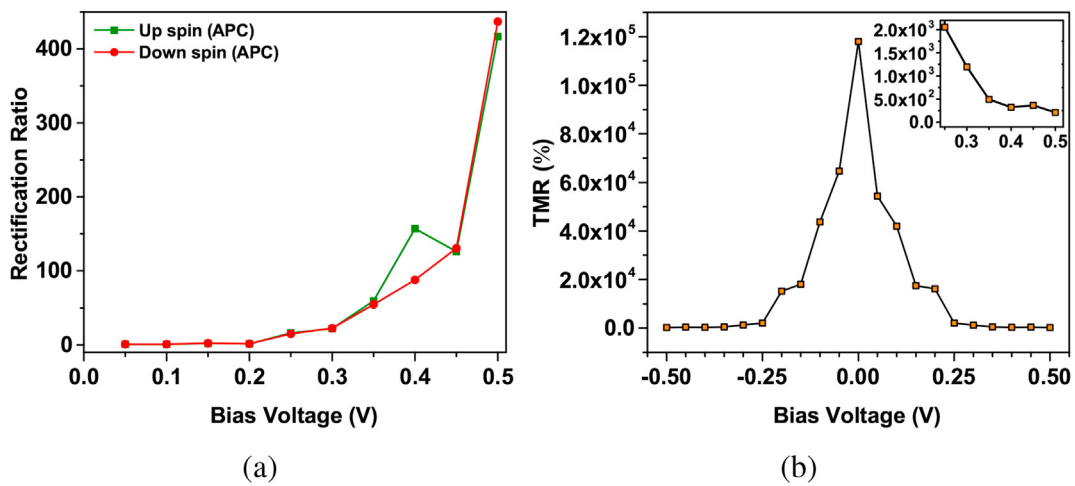(a)　　　　　　　　　　　　　　　　　　　　　　　　　(b)

Fig. 5. (a) Rectification ratio in APC and (b) tunnel magnetoresistance (TMR) of the model device as a function of bias voltage.

$$TMR = \frac{(T_{APC-\alpha} + T_{APC-\beta})^{-1} - (T_{PC-\alpha} + T_{PC-\beta})^{-1}}{(T_{PC-\alpha} + T_{PC-\beta})^{-1}} \times 100\% \quad (7)$$

Here $T_{PC-\alpha/\beta}$ and $T_{APC-\alpha/\beta}$, correspond to the transmission peaks at the Fermi level for majority/minority spin component in PC and APC at zero bias, respectively. The bias-dependent TMR of the device having length L = 24.91 Å is plotted in Fig. 5b. Here, the TMR gradually decreases with the applied bias potential, and the highest value of TMR (1.2×10^5%) is observed at zero bias, which indicates a perfect TMR effect. The TMR value remains significantly large ($> 10^4$%) under the bias range of [-0.2 V, 0.2 V], suggesting the

possibility of modeled device utilization as an organic spin valve. Beyond ± 0.2 V, the TMR decreases slowly as shown in the inset of Fig. 5b for positive bias region. This can be attributed to the abrupt rise (fall) in the total current in APC (PC), which further reduces the TMR. The bias-dependent TMR is symmetric about 0 V, owing to the symmetry in total current for both PC and APC, irrespective of the contributions from different spin-components.

To further explain the high TMR value and perfect filtering at zero bias, the maximum transmission coefficient at the Fermi level (T(E$_F$)$_{Max}$), quantum conductance (G), and transmission eigenvalues are listed in Table 1. The maximum transmission coefficient at the Fermi level (T(E$_F$)$_{Max}$) has been extracted from the transmission

spectrum plot shown in Fig. 2. The zero bias quantum conductance (G) is calculated using the expression 8 given below,

$$G = G_0 T(E, V_b) \qquad (8)$$

Here, G_0 indicates a quantum conductance unit given by $G_0 = \frac{e^2}{2h}$. The transmission eigenvalues are acquired by diagonalizing the transmission matrix, which represent the true transmission probabilities with a range of 0−1. The magnitude of an eigenvalue predicts the respective channel's strength, and the number of eigenvalues provides the number of available channels. It may also exceed the value of one, if multiple channels are available at a specific energy, as it is obtained by adding up the transmission eigenvalues of all the channels available at that particular energy.

For the up spin channel in the PC, the T $(E_F)_{Max}$ attains a value of 0.878, which is relatively large in the context of quantum transport and suggests quasi-ballistic nature [39]. Thus, from a physical point of view, it can be concluded that the incoming wave function from the left electrode reaches to the right electrode with minimum scattering. However, for the down spin channel in PC, the T $(E_F)_{Max}$ and corresponding eigenvalue are significantly low in comparison to the up spin channel, suggesting low and diminished transmission strength for the down spin channel. To support the above statement, the transmission eigenstates at the corresponding eigenvalue have been plotted in Fig. 6, at an isovalue of 0.1. The periodic color map has been used for the isosurface plot, where the color of isosurface represents the phase of a wave function, which is periodic by nature. For up spin channel in the PC, the isosurface plot shows complete delocalization of eigenstates over the central region, indicating pronounced transmission between the electrodes at a particular energy. However, in the spin down channel, the eigenstates are localized in the left side of the central region, prohibiting the propagation of electronic states from left to right electrode. Hence, the transmission through central region for PC is mostly dominated by the up spin channel, which is also in accordance with the magnitude of the eigenvalue. For both the up and down spin channels in APC, the T $(E_F)_{Max}$ and eigenvalues are very small. Therefore, the wave function from the left electrode decays along the transport (z-axis) direction before reaching the right electrode, resulting in low quantum conductance of the device (see Table 1). The same is also true for the down spin channel in PC. It can be seen from the equations (4) and (7) that the massive difference in T $(E_F)_{Max}$ and G at zero bias for the PC and APC results in the perfect filtering and high TMR ratio. Thus, we can conclude from the above analysis that the modeled device projects itself as a potential candidate for the multifunctional spin-based devices, viz. spin filter and dual spin diode in PC and APC, respectively, and also as an organic spin valve. Furthermore, the effect of barrier thickness on the TMR and η by varying the length of trans-polyacetylene has been investigated. The outcomes are similar to that reported elsewhere [40] and follows the

Julliere's model [41] (See supplementary information for the detailed explanation and Fig. S3).

3.2. Impact of hybridization and torsion defects

To address the impact of hybridization as well as torsion defects on the device, the altered (defect induced) models are examined for their spin-dependent transport properties and associated parameters. For further analysis, a defined nomenclature has been used and listed in Table 2. Here, Model IIA is designed by introducing excess hydrogen passivation of two neighboring carbon atoms of Model I at the defect site (as encircled in Fig. 1), which changes the hybridization of both carbon atoms from sp^2 to sp^3. Model IIB possess same atomic configuration as model IIA, but with a different three-dimensional conformation due to torsion at the defect site, resulting in a twisted molecular channel. This torsion affects the energy minimum of molecule IIB in comparison to that of molecule IIA [23].

The I−V characteristics of the altered models IIA and IIB in the PC are shown in Fig. S4(b) and S6(b), respectively (See supplementary information, Fig. S4 and S6). Both the models IIA and IIB show a non-linear curve for the up spin current, while the down spin current is completely suppressed within the considered bias range, thus exhibiting a spin filtration behavior. The total current through model IIA in PC is about 10 times lower than its pristine (Model I) counterpart at 0.5 V, which indicates a decline in the current after introducing the hybridization defect. The current through model IIB is lowered by about 43 times in comparison to model I, indicating a further decrement in the current after introducing both hybridization as well as torsion defects. The current through model IIB is about 4 times lower than the model IIA at 0.5 V, which suggests that the geometrical torsion alone resulted in 4 times decrement in the current, owing to the increased carrier scattering in the central region. Similar to model I, model IIA also shows a NDR behavior for the up spin current in the bias window of 0.3 V−0.35 V with a peak to valley ratio of 1.963. To further justify the spin filtration effect, the η has been calculated for both the models in the PC, using equations (3) and (4). Fig. 7a and d show the variation of η with applied bias voltage for models IIA and IIB, respectively. Here, the value of η remains stable in the range of [98.5, 100] for model IIA and [92.9, 99.99] for model IIB. Moreover, the variation in η is in-line with the modest increment of down spin current (PC) for model IIA

Table 2
Nomenclature used for device models with defects.

Name	Central Region of the Device
Model I	Pristine Trans-polyacetylene
Model IIA	Trans-polyacetylene with hybridization defect
Model IIB	Trans-polyacetylene with hybridization and torsion defects

(a)   (b)
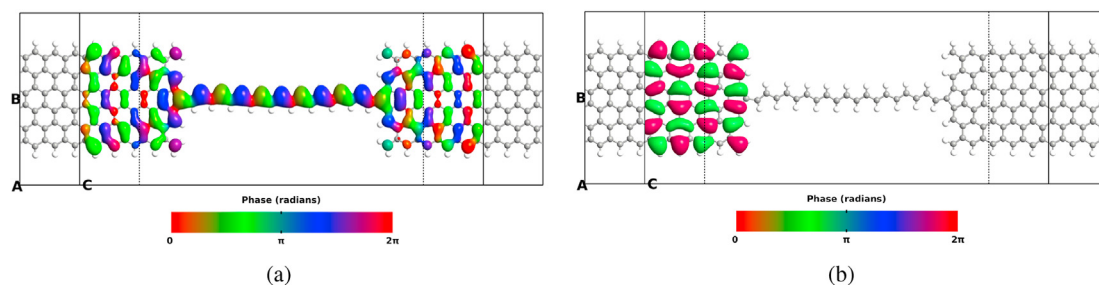
Fig. 6. Transmission eigenstates at an isovalue of 0.1 in PC for (a) up spin and (b) down spin channels.
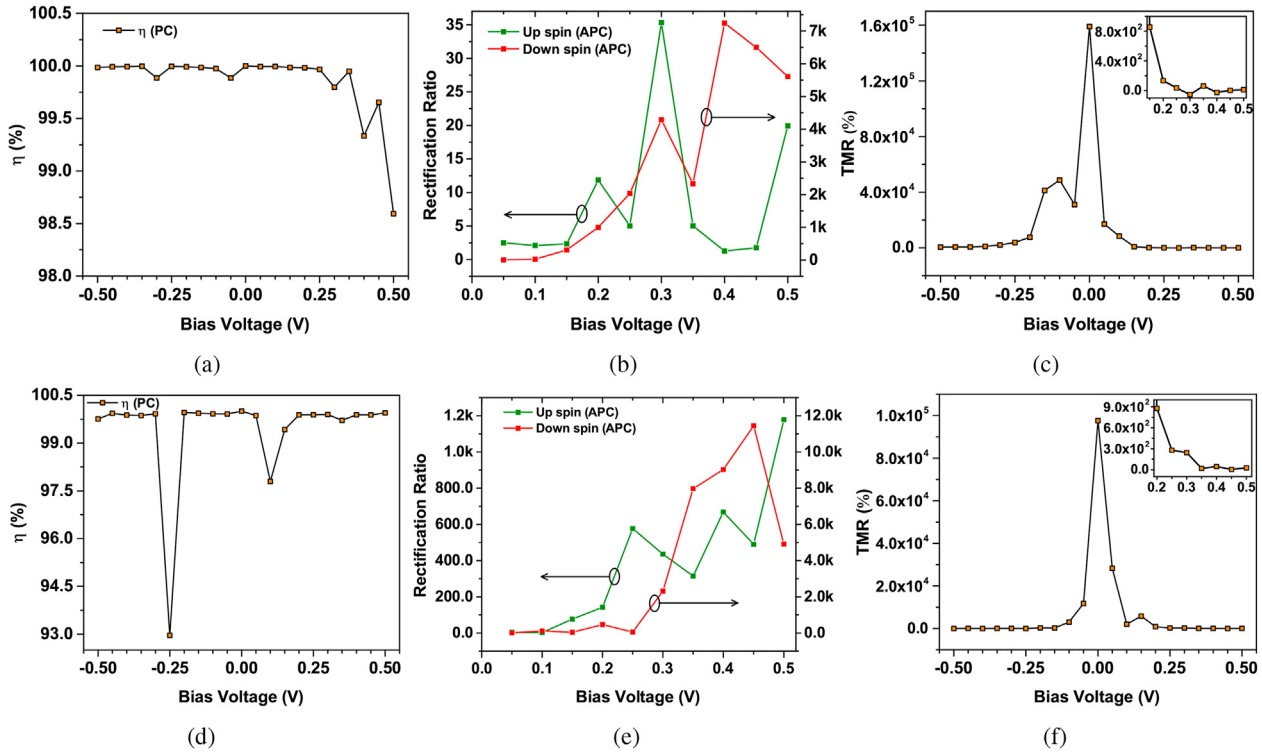
Fig. 7. [(a) and (d)] Spin filtration efficiency (η) in PC, [(b) and (e)] rectification ratio in APC, and [(c) and (f)] tunnel magnetoresistance (TMR) for Model IIA and IIB as a function of bias voltage, respectively. [(a), (b) and (c)] and [(d), (e) and (f)] corresponds to Model IIA and IIB, respectively.

and IIB; as it can be seen from the equation (3) that a rise in the down spin current reduces the η value. This can be better visualized by plotting the area enclosed by the transmission coefficient (T(E)) curve for the applied bias potentials. As seen from Fig. S5(a) (See supplementary information, Fig. S5), the area enclosed by the down spin component increases in the positive bias side, leading to a decline in η for model IIA. Likewise, comment can also be made on the trend followed by η of model IIB from Fig. S7(a) (See supplementary information, Fig. S7).

In APC, the altered models exhibit a spin rectification behavior for both the spin components (See supplementary information, Fig. S4(c) and S6(c)). Model IIA shows a spin rectification behavior for both the up and down spin components on the positive bias side. However, model IIB shows a dual spin rectifying effect with the up spin current inhibited completely in the positive bias side and the down spin current raising beyond 0.15 V; whereas the opposite phenomenon is true for the negative bias side. The total current through model IIA in APC is about 4 times lower than its pristine (Model I) counterpart at 0.5 V, indicating a decline in the current on incorporation of hybridization defect. The current through model IIB is about 17 times lower than model I, indicating a further decline in the current on incorporation of both hybridization and torsion defects. The current through model IIB is about 5 times lower than model IIA at 0.5 V, which suggests that the geometrical torsion alone resulted in 5 times decrement of current. Furthermore, the rectification ratio has been computed for both the models in the APC using equation (5). Fig. 7b and e show the variation of rectification ratio with applied potentials for model IIA and IIB, respectively. The peak rectification ratio for model IIA within the bias window is 35.32 (at 0.3 V) and 7.2 k (at 0.4 V) for up and down spin components, respectively. Meanwhile, model IIB has the peak rectification ratio of 1.2 k (at 0.5 V) and 11.4 k (at 0.45 V) for up and down spin components, respectively. The trend of peak

rectification ratio shows that the up spin component of models IIA and IIB shows about 12 times decrement and about 3 times increment w.r.t its pristine counterpart (model I), respectively; whereas the down spin component of models IIA and IIB shows an increment about 3 times and 26 times w.r.t model I, respectively. These variations are very well comprehended by the plot showing area enclosed by the different spin components in T(E) (See supplementary information, Fig. S5(b) and S7(b).

Similar to model I, the altered models (IIA and IIB) also exhibit a different spin-dependent I−V characteristics for PC and APC. Therefore, the TMR has been calculated for both the models using equations (6) and (7). The bias-dependent TMR of model IIA and IIB are shown in Fig. 7c and f, respectively. Here, the peak value of TMR at zero bias is 1.59×10^5% for model IIA and 9.76×10^4% for model IIB. The computed TMR value of model IIA at zero bias is about 1.3 times higher than model I; whereas, for model IIB at zero bias is about 1.2 times lower than model I. These variation in the zero bias TMR can be attributed to the presence of hybridization and torsion defects, which have either diminished or amplified $T(E_F)_{Max}$ in the PC and APC (See supplementary information, Table. T1). The present analysis suggests that the incorporation of hybridization and torsion defects decreases the total current and varies the η, rectification ratio, and TMR value.

Finally, to compare the performance of our modeled device with previously reported spin-based devices from literature, the key figure of merits such as the maximum value of spin filtration efficiency (η_{Max}), rectification ratio (RR_{Max}), and tunnel magnetoresistance (TMR_{Max}) have been listed in Table 3.

3.3. Spin seebeck effect

Furthermore, the impact of temperature gradient on the spin-dependent current in PC for model I (pristine) have been

Table 3
Comparison of η_{Max}, RR_{Max}, and TMR_{Max} of the proposed models with various previous literature.

| S No.	Spacer material	η_{Max}	RR_{Max}	TMR_{Max}
1.	MgO layer [42]	−	−	$1.14 \times 10^{43}\%$
2.	Carbon atomic chain [19]	≈100%	−	$1.4 \times 10^5\%$ to $2.4 \times 10^6\%$
3.	CoFeMnSi semiconductor [43]	*	110	$2 \times 10^3\%$
4.	Oligoporphyrin molecule [44]	−99%	−	$4.1 \times 10^4\%$
5.	CrI$_3$ layer [45]	*	−	$1.9 \times 10^4\%$
6.	Functionalized graphene sheet [46]	≈100%	−	$344 \times 10^3\%$
7.	Trans-polyacetylene (Present work)			
	Model I	≈100%	436	$1.2 \times 10^5\%$
	Model IIA	100%	7.2 k	$1.59 \times 10^5\%$
	Model IIB	≈100%	11.4 k	$9.76 \times 10^4\%$

Dash (−) and Star (*) correspond to unreported value and qualitatively good (no numerical value available), respectively.

examined. The temperature gradient (ΔT) is defined as, $\Delta T = T_R - T_L$. Here, T_L is the cold left electrode (source) and T_R is the hot right electrode (drain). Fig. 8a illustrates the computed spin-dependent current as a function of T_L for different ΔT, and Fig. 8b illustrates the same as a function of ΔT for different T_L values. From Fig. 8a, the up spin current is observed to be negative, while the down spin current is positive. This particular behavior of current flow in the modeled device indicates the spin Seebeck effect [47]. The up spin current initially increases and then saturates for the T_L above 500 K, but the down spin current is almost zero till about 300 K. In addition, with an increase in ΔT (20 K, 40 K, and 60 K), the thermal currents also increases with the T_L. Fig. 8b shows the variation in the spin-polarized current with ΔT, for different T_L (250 K, 300 K, 350 K, and 400 K). Here, both the up and down spin current flows in the opposite directions, which further confirms the spin Seebeck effect. The up spin current increases almost linearly in negative direction, whereas the down spin current increases after $\Delta T = 100$ K. Moreover, both the spin components increases with the T_L. In both the cases (as shown in Fig. 8), the magnitude of up spin current is higher than the down spin current when the ΔT or T_L is fixed. This can be attributed to a large number of states available for the conduction of up spin component in comparison to the down spin in the vicinity of Fermi level, as shown in

Fig. 2a of the transmission spectrum plot in the PC at zero bias voltage.

Furthermore, the spin filtration efficiency (η) in the PC has been computed using equations (3) and (4). The η plot w.r.t T_L for different ΔT (20 K, 40 K, and 60 K) is shown in Fig. 9a, where for ΔT = 20 K, 40 K, and 60 K, the η maintains a value of almost 100% till 300 K, 450 K, and 400 K, respectively, after which it gradually decreases. These variations are in line with the rise of down spin current (as shown in Fig. 8a) beyond a certain threshold temperature. Moreover, the η plot with respect to ΔT for different T_L (250 K, 300 K, 350 K, and 400 K) is shown in Fig. 9b. Here, for all the T_L values the η decreases with increasing ΔT, and the steepness (rate) of decrement is proportional to the T_L. From the above results, it can be concluded that the display of temperature gradient-dependent spin Seebeck effect and high spin filtration efficiency makes this model a promising candidate in the field of spin caloritronics. Moreover, the combined benefits of spintronics and thermoelectrics may allow its utilization in the fields of energy conversion and information science [28].

To summarize, the comparison of the present model with other competing models for their potential applications is given in Table .4. The comparison shows that the present device is superior to its other counterparts as a multifunctional spintronic device and is capable of serving in various applications such as spin valve, spin filter, spin diode, spin based oscillator, etc.

(a) (b)
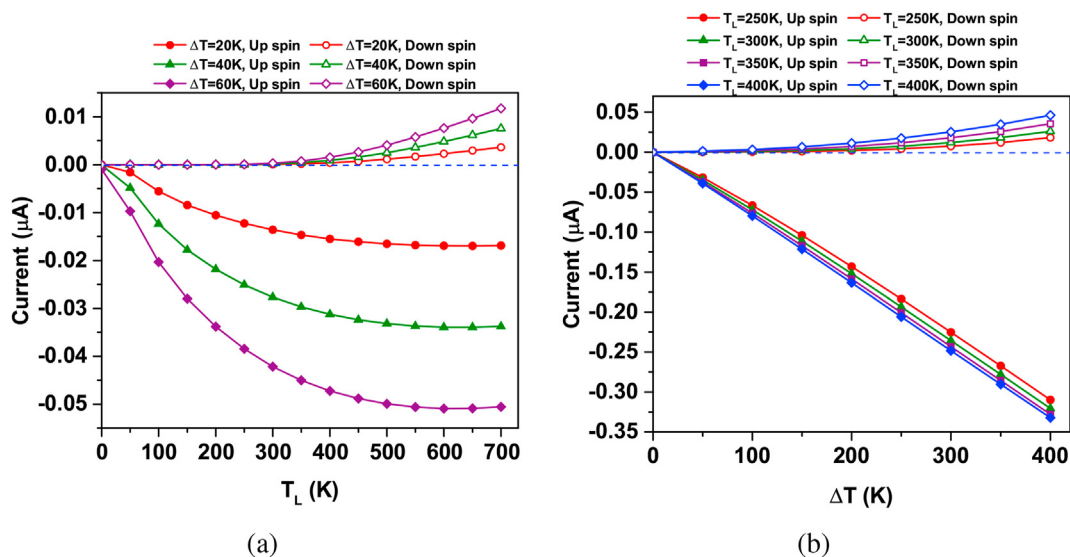
Fig. 8. Thermal spin-dependent currents (a) as a function of T_L at different ΔT and (b) as a function of ΔT at different T_L in PC.
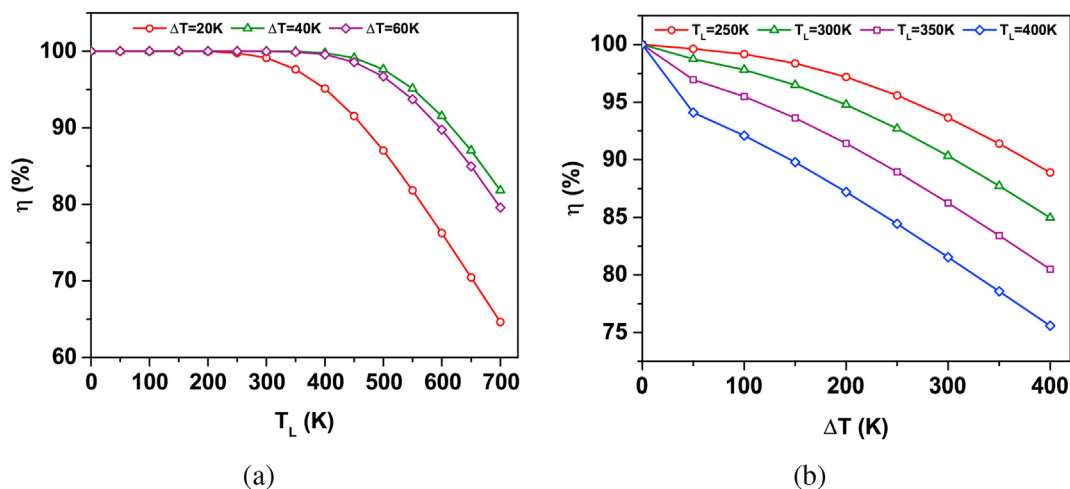
(a)   (b)

Fig. 9. Spin filtration efficiency (η) (a) as a function of T_L at different ΔT and (b) as a function of ΔT at different T_L in the PC.

Table 4
Provisional comparison of the present model with various other competing models for multifunctionality.

Spacer material	Spin Valve	Spin Filter	Spin Diode	NDR	Spin Seebeck Effect
Trans- polyacetylene (Present work)	✓	✓	✓	✓	✓
PTP molecule chain [48]	–	✓	✓	–	–
NTCDI [49]	✓	✓	✓	✓	–
TiO$_2$ [40]	✓	✓	✓	–	–
CrI$_3$ layer [45]	✓	✓	–	–	–
YN$_2$ monolayer [50]	–	✓	✓	–	✓
Oligoporphyrin molecule [44]	✓	✓	–	✓	–
Carbon atomic chain [19]	✓	✓	–	–	–
MgO layer [42]	✓	–	–	–	–

4. Conclusion

The present article discusses the spin-dependent transport phenomenon through a trans-polyacetylene channel sandwiched between two semi-infinite H-passivated ZGNR electrodes. The proposed model exhibits a perfect spin filtering effect in the parallel configuration, dual-spin diode effect, dual-spin filtering effect, and NDR behavior in the antiparallel configuration, along with a large TMR value. The aforementioned peculiar effects are explained with the help of various metrics, such as the area enclosed by the transmission spectrum over the bias potentials, eigenvalues, eigenstates, and quantum conductance. Furthermore, the study shows that the spin-based properties are highly susceptible to the hybridization defect (sp^2 to sp^3 hybridized carbon atoms) and torsion defect in the trans-polyacetylene. Moreover, the spin-dependent current under the influence of temperature gradient has also been analyzed for the pristine device model, in a parallel configuration. The results confirm the presence of the spin Seebeck effect and a high spin filtration efficiency (η). Overall, the analysis suggests that the proposed model can be used as a multi-functional spin-based device in spintronics as well as spin caloritronics applications, such as spin valves, spin filters, spin diodes, and spin oscillators, etc.

Declaration of competing interest

The authors declare that they have no known competing financial interests or personal relationships that could have appeared to influence the work reported in this paper.

Appendix A. Supplementary data

Supplementary data to this article can be found online at https://doi.org/10.1016/j.jsamd.2022.100459.

References

[1] M.E. Flatté, Spintronics, IEEE Trans. Electron Dev. 54 (5) (2007) 907–920, https://doi.org/10.1109/TED.2007.894376.
[2] S.A. Wolf, D. Treger, Spintronics: a new paradigm for electronics for the new millennium, IEEE Trans. Magn. 36 (5 I) (2000) 2748–2751, https://doi.org/10.1109/20.908580.
[3] A. Fert, Nobel lecture: origin, development, and future of spintronics nobel lecture: origin, development, and future of spintronics, Rev. Mod. Phys. 80 (4) (2008) 1517–1530, https://doi.org/10.1103/RevModPhys.80.1517.
[4] M.N. Baibich, J.M. Broto, A. Fert, F.N. Van Dau, F. Petroff, P. Etienne, G. Creuzet, A. Friederich, J. Chazelas, Giant magnetoresistance of (001)Fe/(001)Cr magnetic superlattices, Phys. Rev. Lett. 61 (21) (1988) 2472–2475, https://doi.org/10.1103/PhysRevLett.61.2472. https://link.aps.org/doi/10.1103/PhysRevLett.61.2472.
[5] B. Dieny, V.S. Speriosu, S.S. Parkin, B.A. Gurney, D.R. Wilhoit, D. Mauri, Giant magnetoresistive in soft ferromagnetic multilayers, Phys. Rev. B 43 (1) (1991) 1297–1300, https://doi.org/10.1103/PhysRevB.43.1297.

[6] Z.H. Xiong, D. Wu, Z.V. Vardeny, J. Shi, Giant magnetoresistance in organic spin-valves, Nature 427 (6977) (2004) 821–824, https://doi.org/10.1038/nature02325.

[7] D. Sun, L. Yin, C. Sun, H. Guo, Z. Gai, X.G. Zhang, T.Z. Ward, Z. Cheng, J. Shen, Giant magnetoresistance in organic spin valves, Phys. Rev. Lett. 104 (23) (2010) 1–4, https://doi.org/10.1103/PhysRevLett.104.236602.

[8] S. Datta, B. Das, Electronic analog of the electro-optic modulator, Appl. Phys. Lett. 56 (7) (1990) 665–667, https://doi.org/10.1063/1.102730.

[9] Y. G. Semenov, K. W. Kim, J. M. Zavada, Spin field effect transistor with a graphene channel, Appl. Phys. Lett. 91 (15). doi:10.1063/1.2798596.

[10] V. Dediu, M. Murgia, F.C. Matacotta, C. Taliani, S. Barbanera, Room temperature spin polarized injection in organic semiconductor, Solid State Commun. 122 (3–4) (2002) 181–184, https://doi.org/10.1016/S0038-1098(02)00090-X.

[11] V.A. Dediu, L.E. Hueso, I. Bergenti, C. Taliani, Spin routes in organic semiconductors, Nat. Mater. 8 (9) (2009) 707–716, https://doi.org/10.1038/nmat2510.

[12] W. J. Naber, S. Faez, W. G. Van Der Wiel, Organic spintronics, J. Phys. Appl. Phys. 40 (12). doi:10.1088/0022-3727/40/12/R01.

[13] L. Guo, Y. Qin, X. Gu, X. Zhu, Q. Zhou, X. Sun, Spin transport in organic molecules, Front. Chem. 7 (JUN) (2019) 1–11, https://doi.org/10.3389/fchem.2019.00428.

[14] A.R. Rocha, V.M. García-Suárez, S.W. Bailey, C.J. Lambert, J. Ferrer, S. Sanvito, Towards molecular spintronics, Nat. Mater. 4 (4) (2005) 335–339, https://doi.org/10.1038/nmat1349.

[15] N. Zheng, Z. Lin, Y. Zheng, D. Li, J. Yang, W. Zhang, L. Wang, G. Yu, Room-temperature stable organic spin valves using solution-processed ambipolar naphthalenediimide-based conjugated polymers, Org. Electron. 81 (February) (2020) 105684, https://doi.org/10.1016/j.orgel.2020.105684.

[16] X. Sun, A. Bedoya-Pinto, Z. Mao, M. Gobbi, W. Yan, Y. Guo, A. Atxabal, R. Llopis, G. Yu, Y. Liu, A. Chuvilin, F. Casanova, L.E. Hueso, Active morphology control for concomitant long distance spin transport and photoresponse in a single organic device, Adv. Mater. 28 (13) (2016) 2609–2615, https://doi.org/10.1002/adma.201503831. https://onlinelibrary.wiley.com/doi/abs/10.1002/adma.201503831.

[17] T.D. Nguyen, E. Ehrenfreund, Z.V. Vardeny, Spin-polarized light-emitting diode based on an organic bipolar spin valve, Science 337 (6091) (2012) 204–209, https://doi.org/10.1126/science.1223444. https://science.sciencemag.org/content/337/6091/204.

[18] A.K. Geim, K. Novoselov, P. Blake, Graphene spin valve devices, IEEE Trans. Magn. 42 (10) (2006) 2694–2696, https://doi.org/10.1109/TMAG.2006.878852.

[19] M.G. Zeng, L. Shen, Y.Q. Cai, Z.D. Sha, Y.P. Feng, Perfect spin-filter and spin-valve in carbon atomic chains, Appl. Phys. Lett. 96 (4) (2010) 4–6, https://doi.org/10.1063/1.3299264.

[20] S.A. Sharko, A.I. Serokurova, T.I. Zubar, S.V. Trukhanov, D.I. Tishkevich, A.A. Samokhvalov, A.L. Kozlovskiy, M.V. Zdorovets, L.V. Panina, V.M. Fedosyuk, A.V. Trukhanov, Multilayer spin-valve CoFeP/Cu nanowires with giant magnetoresistance, J. Alloys Compd. 846 (2020) 156474, https://doi.org/10.1016/j.jallcom.2020.156474.

[21] A. Bordoloi, V. Zannier, L. Sorba, C. Schönenberger, A. Baumgartner, A double quantum dot spin valve, Commun. Phys. 3 (1) (2020) 1–7, https://doi.org/10.1038/s42005-020-00405-2.

[22] M. Zhou, H. Jin, Y. Xing, In-plane dual-gated spin-valve device based on the zigzag graphene nanoribbon, Phys. Rev. Appl. 13 (4) (2020) 1, https://doi.org/10.1103/PhysRevApplied.13.044006.

[23] K. Gaurav, B. SanthiBhushan, G. Mino-Galaz, G. Gutierrez, A. Srivastava, Hybridization and torsion defects influenced electron transport in trans-polyacetylene, Phys. E Low-dimens. Syst. Nanostruct. (2021) 114628doi, https://doi.org/10.1016/j.physe.2021.114628. http://www.sciencedirect.com/science/article/pii/S1386947721000102.

[24] J. Simon, J.-J. André, J.M. Lehn, C.W. Rees, Polyacetylene, Springer Berlin Heidelberg, Berlin, Heidelberg, 1985, pp. 150–200, https://doi.org/10.1007/978-3-642-70012-5_4.

[25] J. Jiang, X. Lang, Q. Zeng, M.B. Faheem, S. Rong, H. Zhao, Y. Li, Polyacetylene derivatives in perovskite solar cells: from defect passivation to moisture endurance, J. Mater. Chem. 9 (22) (2021) 13220–13230, https://doi.org/10.1039/D0TA12509A.

[26] B.R. Boswell, C.M.F. Mansson, J.M. Cox, Z. Jin, J.A.H. Romaniuk, K.P. Lindquist, L. Cegelski, Y. Xia, S.A. Lopez, N.Z. Burns, Mechanochemical synthesis of an elusive fluorinated polyacetylene, Nat. Chem. 13 (1) (2021) 41–46, https://doi.org/10.1038/s41557-020-00608-8.

[27] G.E.W. Bauer, E. Saitoh, B.J. van Wees, Spin caloritronics, Nat. Mater. 11 (5) (2012) 391–399, https://doi.org/10.1038/nmat3301.

[28] N. Pandey, A. Kumar, S. Chakrabarti, First principle study of temperature-dependent magnetoresistance and spin filtration effect in WS2 nanoribbon, ACS Appl. Mater. Interfaces 11 (42) (2019) 39248–39253, https://doi.org/10.1021/acsami.9b10618.

[29] W. Koch, M.C. Holthausen, A Chemist's Guide to Density Functional Theory, Wiley VCH, Weinheim - New York, https://onlinelibrary.wiley.com/doi/book/10.1002/3527600043.

[30] M. Brandbyge, J.-L. Mozos, P. Ordejón, J. Taylor, K. Stokbro, Density-functional method for nonequilibrium electron transport, Phys. Rev. B 65 (16) (2002) 165401, https://doi.org/10.1103/PhysRevB.65.165401.

[31] S. Smidstrup, T. Markussen, P. Vancraeyveld, J. Wellendorff, J. Schneider, T. Gunst, B. Verstichel, D. Stradi, P.A. Khomyakov, U.G. Vej-Hansen, M.-E. Lee, S.T. Chill, F. Rasmussen, G. Penazzi, F. Corsetti, A. Ojanperä, K. Jensen, M.L.N. Palsgaard, U. Martinez, A. Blom, M. Brandbyge, K. Stokbro, QuantumATK: an integrated platform of electronic and atomic-scale modelling tools, J. Phys. Condens. Matter 32 (1) (2019) 15901, https://doi.org/10.1088/1361-648x/ab4007.

[32] J.P. Perdew, K. Burke, M. Ernzerhof, Generalized gradient approximation made simple, Phys. Rev. Lett. 77 (18) (1996) 3865–3868, https://doi.org/10.1103/PhysRevLett.77.3865.

[33] H.D. Cornean, A. Jensen, V. Moldoveanu, A rigorous proof of the Landauer-Büttiker formula, J. Math. Phys. 46 (4) (2005) 42106, https://doi.org/10.1063/1.1862324.

[34] A. Akbari-Sharbaf, S. Ezugwu, M.S. Ahmed, M.G. Cottam, G. Fanchini, Doping graphene thin films with metallic nanoparticles: experiment and theory, Carbon 95 (2015) 199–207, https://doi.org/10.1016/j.carbon.2015.08.021. https://www.sciencedirect.com/science/article/pii/S0008622315301408.

[35] S. Singh, I. Kaur, Bandgap engineering in armchair graphene nanoribbon of zigzag-armchair-zigzag based Nano-FET: a DFT investigation, Phys. E Low-dimens. Syst. Nanostruct. 118 (2020) 113960, https://doi.org/10.1016/j.physe.2020.113960. https://www.sciencedirect.com/science/article/pii/S1386947719314420.

[36] P. Kumari, S. Majumder, S. Rani, A.K. Nair, K. Kumari, M.V. Kamalakar, S.J. Ray, High efficiency spin filtering in magnetic phosphorene, Phys. Chem. Chem. Phys. 22 (10) (2020) 5893–5901, https://doi.org/10.1039/c9cp05390e.

[37] E. Alekseev, D. Pavlidis, Large-signal microwave performance of GaN-based NDR diode oscillators, Solid State Electron. 44 (6) (2000) 941–947, https://doi.org/10.1016/S0038-1101(00)00011-3. https://www.sciencedirect.com/science/article/pii/S0038110100000113.

[38] X. Feng, O. Bengone, M. Alouani, I. Rungger, S. Sanvito, Interface and transport properties of Fe/V/MgO/Fe and Fe/V/Fe/MgO/Fe magnetic tunneling junctions, Phys. Rev. B 79 (21) (2009) 214432, https://doi.org/10.1103/PhysRevB.79.214432. https://link.aps.org/doi/10.1103/PhysRevB.79.214432.

[39] Y. Kruglyak, M. Strikha, Landauer - Datta - Lundstrom generalized electron transport model for micro- and nanoelectronics, in: 2015 IEEE 35th International Conference on Electronics and Nanotechnology, (ELNANO), 2015, pp. 70–74, https://doi.org/10.1109/ELNANO.2015.7146837.

[40] J. Han, J. Shen, G. Gao, CrO 2 -based heterostructure and magnetic tunnel junction: perfect spin filtering effect, spin diode effect and high tunnel magnetoresistance, RSC Adv. 9 (7) (2019) 3550–3557, https://doi.org/10.1039/c8ra08107g.

[41] M. Julliere, Tunneling between ferromagnetic films, Phys. Lett. 54 (3) (1975) 225–226, https://doi.org/10.1016/0375-9601(75)90174-7. https://www.sciencedirect.com/science/article/pii/0375960175901747.

[42] S. Ikeda, J. Hayakawa, Y. Ashizawa, Y.M. Lee, K. Miura, H. Hasegawa, M. Tsunoda, F. Matsukura, H. Ohno, Tunnel magnetoresistance of 604% at 300K by suppression of Ta diffusion in CoFeBMgOCoFeB pseudo-spin-valves annealed at high temperature, Appl. Phys. Lett. 93 (8) (2008) 82508, https://doi.org/10.1063/1.2976435.

[43] J. Han, Y. Feng, K. Yao, G. Y. Gao, Spin transport properties based on spin gapless semiconductor CoFeMnSi, Appl. Phys. Lett. 111 (13). doi:10.1063/1.4999288.

[44] P. Zhao, X.J. Gao, Y. Song, X.X. Li, G. Chen, Spin-filtering, giant magnetoresistance, negative differential resistance effects and spin logic gate in P2TA-O2-based molecular junction with different transition metal atoms, Org. Electron. 57 (January) (2018) 104–109, https://doi.org/10.1016/j.orgel.2018.03.007.

[45] T. Song, X. Cai, M.W.-Y. Tu, X. Zhang, B. Huang, N.P. Wilson, K.L. Seyler, L. Zhu, T. Taniguchi, K. Watanabe, M.A. McGuire, D.H. Cobden, D. Xiao, W. Yao, X. Xu, Giant tunneling magnetoresistance in spin-filter van der Waals heterostructures, Science 360 (6394) (2018) 1214–1218, https://doi.org/10.1126/science.aar4851. https://www.science.org/doi/abs/10.1126/science.aar4851.

[46] N. Pandey, A. Kumar, S. Chakrabarti, Tunnelling magnetoresistance and spin filtration effect in functionalized graphene sheet with CrO2 as electrode: an ab-initio study, J. Magn. Magn Mater. 497 (October 2019) (2019) 2, https://doi.org/10.1016/j.jmmm.2019.166073.

[47] K. Uchida, S. Takahashi, K. Harii, J. Ieda, W. Koshibae, K. Ando, S. Maekawa, E. Saitoh, Observation of the spin Seebeck effect, Nature 455 (7214) (2008) 778–781, https://doi.org/10.1038/nature07321.

[48] T. Chen, W. Ding, H. Li, G. Zhou, Length-independent multifunctional device based on penta-tetra-pentagonal molecule: a first-principles study, J. Mater. Chem. C 9 (10) (2021) 3652–3660, https://doi.org/10.1039/D0TC05488G.

[49] W. Ma, W. Wang, Y. Huang, T. Zhou, S. Wang, A multi-functional spintronic device based on 1,4,5,8-naphthalenetetracarboxylic diimide, Comput. Theor. Chem. 1198 (2021) 113170, https://doi.org/10.1016/j.comptc.2021.113170. https://www.sciencedirect.com/science/article/pii/S2210271X21000293.

[50] J. Li, G. Gao, Y. Min, K. Yao, Half-metallic YN2 monolayer: dual spin filtering, dual spin diode and spin Seebeck effects, Phys. Chem. Chem. Phys. 18 (40) (2016) 28018–28023, https://doi.org/10.1039/c6cp05626a.